AIAA SciTech Forum
9 - 13 January 2017, Grapevine, Texas
AIAA Guidance, Navigation, and Control Conference
10.2514/6.2017-1030

Lost in Space and Time

V. Hunter Adams* and Mason Peck†

This paper considers a novel method for autonomously recovering spacecraft position, velocity, and the time using measurements from onboard cameras and a timer. The spacecraft in question is traveling in the vicinity of the Earth and Moon and has lost knowledge of its trajectory through space and time. Batched measurements are used to reduce the searchspace substantially enough to instantiate a particle filter that converges to the true spacecraft trajectory. Using the method described in this paper, the time can be recovered to within tens of minutes and the trajectory to within tens of kilometers from extremely limited prior knowledge.

Nomenclature

x	x component of the position vector $\mathbf{r}$ in Earth-Centered Inertial (ECI) frame (km)
y	y component of the position vector $\mathbf{r}$ in ECI frame (km)
z	z component of the position vector $\mathbf{r}$ in ECI frame (km)
t	Current time (sec)
t_0	Initial time
$\mathbf{r}$	Position vector in ECI frame (km)
$\mathbf{x}$	State vector
r	Radius (km)
μ	Graviatational paramameter (km^3/sec^2)
ρ	Separation distance (km)
d	Time-dependent celestial body position from ephemerides (km)
P	Pixel-width of camera field of view (pixels)
Θ	Camera field of view (radians)
δ	Standard deviation of centroid measurement error
Δ	Standard deviation of elapsed time measurement error
R	Measurement error covariance matrix
Q	Process noise covariance matrix
ν	Innovation
χ	Particle, defined by position, velocity, time, and initial time

Subscript

e	Earth
m	Moon
s	Sun
ec	Earth to spacecraft
em	Earth to Moon
es	Earth to Sun
cs	Spacecraft to Sun
cm	Spacecraft to Moon
mx	x-position, Moon (ECI)
my	y-position, Moon (ECI)
mz	z-position, Moon (ECI)

*Graduate Research Assistant, Sibley School of Mechanical and Aerospace Engineering, 127 Upson Hall, Ithaca NY 14853, AIAA Student Member

†Associate Professor, Sibley School of Mechanical and Aerospace Engineering, 212 Upson Hall, Ithaca NY 14853, AIAA Senior Member

sx	x-position, Sun (ECI)
sy	y-position, Sun (ECI)
sz	z-position, Sun (ECI)

Superscript

T	Transposed
e	Ephemeral frame

I. Introduction

The rapid improvement of commercial-off-the-shelf (COTS) hardware has enabled low-Earth-orbit (LEO) spacecraft missions at a fraction of the cost that was typical just a decade ago. Furthermore, the dramatic performance improvements in COTS components means that spacecraft are no longer the purview of governments and government contractors alone, but also of universities, startups, and hobbyists. It might be argued that this trend has been around as long as the Space Age, starting with OSCAR and other amateur-radio spacecraft. Companies like AeroAstro and Surrey Space Technologies certainly helped bring it about. But most would agree that this revolution took hold thanks to the creation of the CubeSat standard in roughly 2000. The cutting edge of this paradigm is now the current Sprite chipsat, a $30 printed-circuit-board (PCB) spacecraft with nearly all of its subsystems adapted from the cell phone and gaming industries[4]. This new generation of spacecraft offers nearly as many challenges, however, as it does opportunities.

One such challenge is that small form-factor spacecraft lack the power-generating surface area of their larger counterparts, making deep-space and interplanetary missions particularly difficult. These power restrictions limit the communications capabilities of many CubeSats and other small-scale spacecraft, which precludes navigation by means of traditional Earth-based ranging resources. Furthermore, the cost of using existing ranging capabilities is out of proportion to that of the overall mission, which is likely no more than a million USD for all but the most expensive government-built CubeSats. It is partly for this reason that NASA identified deep-space communications as a technology gap in the 2014 Small Spacecraft Technology State of the Art report[5]. There is a need for a method of autonomous navigation for this new generation of spacecraft.

One particularly compelling option is optical navigation, various aspects of which have been studied by a number of researchers. Liounis, Daniel, and Christian consider a manned spacecraft in the Earth-Moon system that must autonomously navigate back to Earth using optical observations of the Earth, Moon, and stars [3]. Their algorithm involves an image filter on features of the celestial bodies that feeds an Extended Kalman Filter (EKF), which converges to the spacecraft trajectory. The filter converges to within 66 meters of true spacecraft position and 1.5 cm/sec of true velocity for a 100 km circular lunar orbit. For the situation treated in this paper, the lack of time knowledge and the trans-lunar trajectory under consideration preclude the use of a similar EKF, which requires a known dynamics model. Furthermore, this analysis assumes cheap, COTS cameras that lack the resolution and contrast required to disambiguate any features on any celestial body, or to gather any information at all about stars other than the Sun. In [2], Lightsey and Christian develop an image-processing algorithm for an onboard optical system. The algorithm calculates the apparent centroid and diameter of a celestial body and calculates the relative angle between a body horizon and a reference star. The present study assumes that a similar sort of image processing procedure has already taken place and uses this a priori information to determine spacecraft trajectory and time.

A similar problem to that treated in this paper was addressed for Deep Space 1, the first interplanetary spacecraft of NASAs New Millennium program. The spacecraft used onboard cameras to sight up to 12 asteroids at a time and used those sightings in a least-squares filter to estimate the spacecraft orbital parameters. The ephemerides for each body are assumed to be known a priori, and errors in the ephemerides are minimized by combining information from all observed asteroids. Monte Carlo simulation shows convergence to true position to within approximately 95 km, and convergence to true velocity to within approximately 0.2 m/s[1]. As with other previous research, the authors assume knowledge of time which provides a known dynamics model.

This work departs from existing research in that it considers the situation in which the spacecraft must recover not only its position and velocity but also the absolute time. Since time dictates the position of the gravitational bodies and thus the dynamic equations for the spacecraft, conventional filters like the EKF and sigma-point filter cannot be immediately employed. It is critically important that fully autonomous COTS spacecraft be able to recover their state, including the time, after an interruption in normal operations without expending the power necessary to communicate with an Earth-based ranging resource. Such a capability could help enable previously power-prohibitive deep-space missions to be performed by CubeSats and similarly small, COTS spacecraft. It could also benefit any spacecraft with time-sensitive operations that cannot count on the ground to correct an on-board clock.

II. Problem Statement

The spacecraft of interest is traveling in the vicinity of the Earth and Moon and has lost knowledge of its trajectory through both space and time. The spacecraft has no means of communicating with the Deep Space Network or other Earth-based ranging facilities, but it carries onboard cameras that provide digital images of the Earth, Sun, and Moon. A clock measures time elapsed since starting the recovery procedure, and an on-board ephemeris for each celestial body is available to provide high-precision knowledge of the vectors relating their position for each moment in the mission lifetime of the spacecraft. Futhermore, the planned mission trajectory is taken to be stored in spacecraft memory. The spacecraft may drift by many thousands of kilometers from the intended trajectory, but this ob-board trajectory plan provides general information regarding the planned position of the spacecraft at a given time. This paper considers a novel method for autonomously recovering spacecraft position, velocity, and the time provided these optical measurements of the Earth, Sun, and Moon. The image-processing aspect of this problem is not treated; it is assumed that an algorithm similar to that in [2] provides the necessary information from an image. This paper focuses on using that information to determine spacecraft trajectory through space and time.

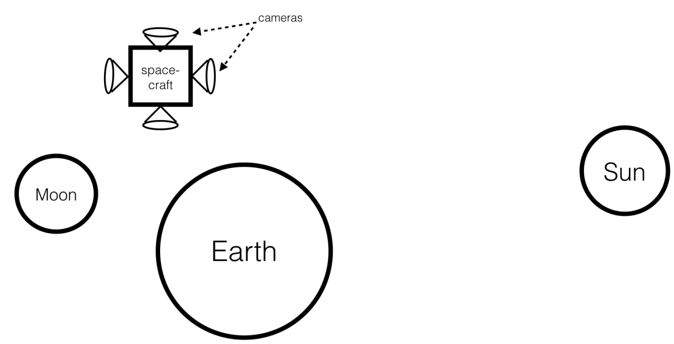

Figure 1. Spacecraft adrift in cislunar space

III. Dynamics Model

The recovery procedure described in this paper is robust to trajectories with significant stochastic effects from unmodeled dynamics, thruster misalignment, etc. For realism, however, it is assumed that the spacecraft enters a safe mode after losing knowledge of time and trajectory. In such a mode, the thrusters do not fire, and the spacecrafts dynamics dominated by the gravitational influences of the Earth, Sun, and Moon. As a particular example, this paper considers the trans-lunar trajectory shown in Fig. 2. The mission begins December 15, 2017 and lasts for 75 days. The positions of the celestial bodies come from the Jet Propulsion Labs HORIZONS ephemeris tables. The state variables include the spacecraft position and velocity, along with the current time and the time at which the recovery process begins.

$$\mathbf{x} = \begin{bmatrix} x & y & z & \dot{x} & \dot{y} & \dot{z} & t & t_0 \end{bmatrix}^T \tag{1}$$

$$= \begin{bmatrix} \mathbf{r}_{ec} & \dot{\mathbf{r}}_{ec} & t & t_0 \end{bmatrix}^T \tag{2}$$

The dynamics for each of these state variables is given by eqns. 3-5. J2 and higher-order effects are omitted, along with perturbing forces. Because of the robustness of particle filters to unmodeled dynamics, this simplification does not significantly affect the performance of the recovery algorithm. And regardless of the filter, J2 and other Earth-specific effects are less significant in cislunar space.

$$\ddot{\mathbf{r}}_{ec} = -\frac{\mu_e}{(\mathbf{r}_{ec}^T\mathbf{r}_{ec})^{\frac{3}{2}}}\mathbf{r_{ec}} + \mu_m\left(\frac{\mathbf{r}_{em} - \mathbf{r}_{ec}}{(\mathbf{r}_{cm}^T\mathbf{r}_{cm})^{\frac{3}{2}}} - \frac{\mathbf{r}_{em}}{\rho_{em}^3}\right) + \mu_s\left(\frac{\mathbf{r}_{es} - \mathbf{r}_{ec}}{(\mathbf{r}_{cs}^T\mathbf{r}_{cs})^{\frac{3}{2}}} - \frac{\mathbf{r}_{es}}{\rho_{es}^3}\right) \tag{3}$$

$$\dot{t} = 1 \tag{4}$$

$$\dot{t_0} = 0 \tag{5}$$

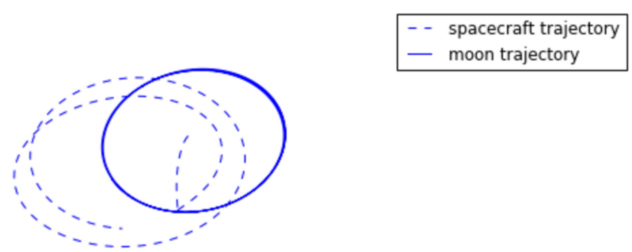

Figure 2. Spacecraft and Moon trajectories

IV. Measurement Model

At each instant when the algorithm needs measurements, all three celestial bodies are taken to be in the field of view of the spacecraft camera system, or their images be propagated forward from the most recent time when they were in the field of view. The measurements are illustrated in fig. 3. One can represent each of these measured quantities in terms of the state variables of interest from Section III. Doing so creates the nonlinear measurement model that relates measured quantities to the state variables, shown in Eq (6). Evaluating this measurement model for each state in the trajectory shown in fig. 2 yields the measurements shown in figs. 4-6.

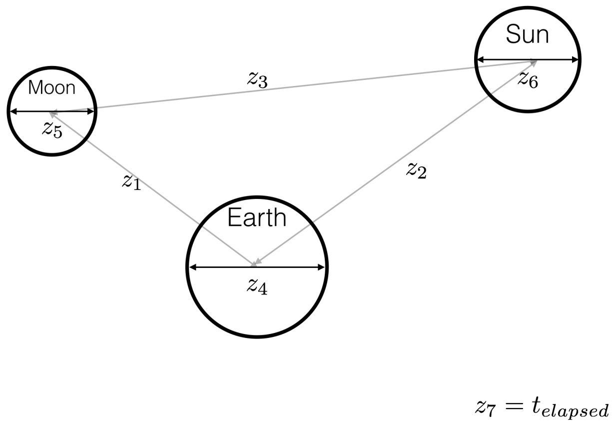

Figure 3. Measured quantities

$$
\begin{aligned}
z_1 &= \cos^{-1}\left[\frac{-xd_{\mathrm{mx}} - yd_{\mathrm{my}} - zd_{\mathrm{mz}} + (-x)^2 + (-y)^2 + (-z)^2}{\sqrt{(-x)^2 + (-y)^2 + (-z)^2}\sqrt{(d_{\mathrm{mx}} - x)^2 + (d_{\mathrm{my}} - y)^2 + (d_{\mathrm{mz}} - z)^2}}\right]\frac{P}{\Theta} \\
z_2 &= \cos^{-1}\left[\frac{-xd_{\mathrm{sx}} - yd_{\mathrm{sy}} - zd_{\mathrm{sz}} + (-x)^2 + (-y)^2 + (-z)^2}{\sqrt{(-x)^2 + (-y)^2 + (-z)^2}\sqrt{(d_{\mathrm{sx}} - x)^2 + (d_{\mathrm{sy}} - y)^2 + (d_{\mathrm{sz}} - z)^2}}\right]\frac{P}{\Theta} \\
z_3 &= \cos^{-1}\left[\frac{d_{\mathrm{mx}}(d_{\mathrm{sx}} - x) + d_{\mathrm{my}}(d_{\mathrm{sy}} - y) + d_{\mathrm{sz}}(d_{\mathrm{mz}} - z) - zd_{\mathrm{mz}} - xd_{\mathrm{sx}} - yd_{\mathrm{sy}} + (-x)^2 + (-y)^2 + (-z)^2}{\sqrt{(d_{\mathrm{mx}} - x)^2 + (d_{\mathrm{my}} - y)^2 + (d_{\mathrm{mz}} - z)^2}\sqrt{(d_{\mathrm{sx}} - x)^2 + (d_{\mathrm{sy}} - y)^2 + (d_{\mathrm{sz}} - z)^2}}\right]\frac{P}{\Theta} \\
z_4 &= \frac{2P}{\Theta}\tan^{-1}\left(\frac{r_e}{\sqrt{(-x)^2 + (-y)^2 + (-z)^2}}\right) \\
z_5 &= \frac{2P}{\Theta}\tan^{-1}\left(\frac{r_m}{\sqrt{(-x + d_{mx})^2 + (-y + d_{my})^2 + (-z + d_{mz})^2}}\right) \\
z_6 &= \frac{2P}{\Theta}\tan^{-1}\left(\frac{r_s}{\sqrt{(-x + d_{sx})^2 + (-y + d_{sy})^2 + (-z + d_{sz})^2}}\right) \\
z_7 &= t - t_0
\end{aligned}
\tag{6}
$$

In Eq (6), d_{ij} (where $i = m, s$ and $j = x, y, z$) represents the time-dependent x, y, and z position of the Moon and the Sun in an ECI coordinate frame. These quantities come from the onboard ephemeris table for each body, but knowledge of the time is required to pull the quantity from the correct row of the table. z_1, z_2 and z_3 are the pixel separations among the three celestial bodies (Earth/Moon, Earth/Sun, and Moon/Sun, respectively). z_4, z_5, and z_6 are the pixel widths of the three celestial bodies (Earth, Moon, and Sun, respectively), and z_7 is the elapsed time since beginning to recover time and trajectory. All of the nonlinear measurement equations can be stacked to form the nonlinear measurement model shown in Eq (7).

$$
\mathbf{z} = \begin{bmatrix} z_1 \\ z_2 \\ z_3 \\ z_4 \\ z_5 \\ z_6 \\ z_7 \end{bmatrix} = \begin{bmatrix} h_1(\mathbf{x}) \\ h_2(\mathbf{x}) \\ h_3(\mathbf{x}) \\ h_4(\mathbf{x}) \\ h_5(\mathbf{x}) \\ h_6(\mathbf{x}) \\ h_7(\mathbf{x}) \end{bmatrix} = \mathbf{h}(\mathbf{x}) \tag{7}
$$

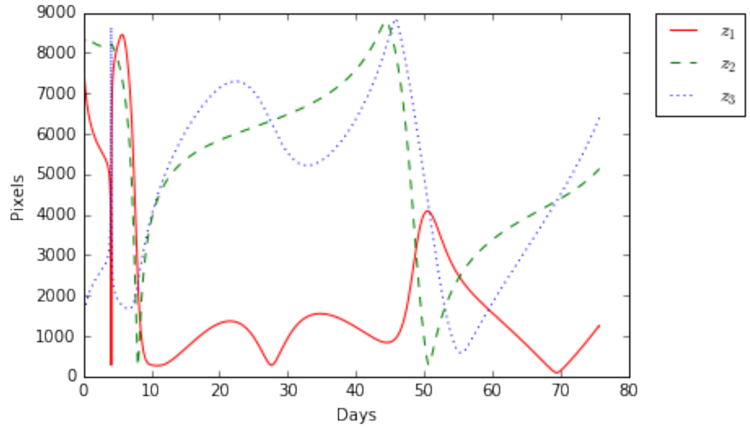

Figure 4. Measured pixel separation among bodies

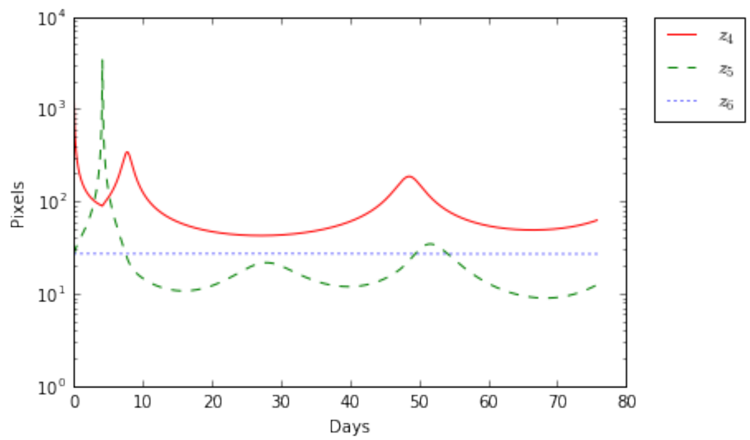

Figure 5. Measured pixel widths of bodies

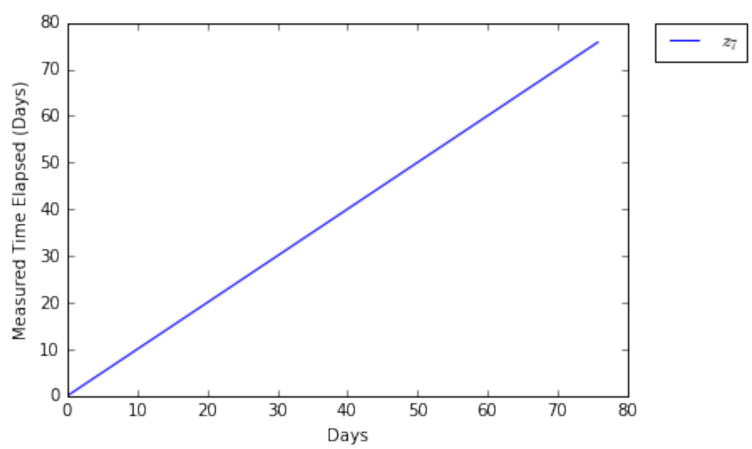

Figure 6. Measured time elapsed

There is noise associated with the above measurements. If one assumes the ability to determine the centroids of the celestial bodies with white Gaussian zero-mean error of standard deviation δ, the centroid determination error can be expressed as shown in Eq (8).

$$E_{centroid} = \mathcal{N}(0, \delta^2) \text{ (measured in pixels)} \tag{8}$$

This information can be used to determine error in the relative pixel separation measurements, which are approximated as independent, and in angular width measurements, which combine independent measurements of the edges of each body.

$$\begin{aligned} E_{separation} &= \mathcal{N}(0, \delta^2) + \mathcal{N}(0, \delta^2) && (9) \\ &= \mathcal{N}(0, 2\delta^2) && (10) \end{aligned}$$

Furthermore, it is assumed that elapsed time measurement error is zero-mean Gaussian with a standard deviation of Δ. For purposes of the example offered in this paper, δ is set to 0.25 pixels and Δ is assumed to be 0.001 seconds. All of this information can be encapsulated in the measurement error covariance matrix R.

$$R = \begin{bmatrix} 2\delta^2 & 0 & 0 & 0 & 0 & 0 & 0 \\ 0 & 2\delta^2 & 0 & 0 & 0 & 0 & 0 \\ 0 & 0 & 2\delta^2 & 0 & 0 & 0 & 0 \\ 0 & 0 & 0 & 2\delta^2 & 0 & 0 & 0 \\ 0 & 0 & 0 & 0 & 2\delta^2 & 0 & 0 \\ 0 & 0 & 0 & 0 & 0 & 2\delta^2 & 0 \\ 0 & 0 & 0 & 0 & 0 & 0 & \Delta^2 \end{bmatrix} \tag{11}$$

V. Search Space Reduction

The objective of the recovery algorithm is to find the correct minimum of the cost function shown in Eq (12). The search space for this problem is extensive. In the example considered here, the spacecraft could be anywhere within 800,000 km of the Earth, traveling at 0-7 km/sec in any direction, at any time in a 75-day period. Properly populating that search space with particles for a particle filter would be prohibitively expensive. Instead, one can use a batch of measurements to cutdown the search space to a series of rings at a discrete number of times. By evaluating the cost of each point that composes each ring, one can find the least-costly (most likely) locations for the spacecraft in space and time. By comparing these locations, which are generally separated by tens of thousands of kilometers and multiple days, to the expected locations from the planned trajectory, one can select the proper point with which to seed a particle filter.

$$J(\mathbf{x}) = \frac{1}{2}\left[\mathbf{z} - h(\mathbf{x})\right]^T R^{-1}\left[\mathbf{z} - h(\mathbf{x})\right] \tag{12}$$

The searchspace through time can be reduced by forming rough approximations of the distance from the Earth to the Moon. A batch of measurements leads to an approximation for the mean and variance of those measurements and generate a distribution for width of the Earth, width of the Moon, and separation between Earth and Moon. Each measurement in that distribution can be converted from pixels to kilometers and radians via Eqs (13-15), which generates distributions for distance to the Earth, distance to the Moon, and separating angle in radians (figs. 7-9).

$$\rho_{ce} \approx \frac{r_e}{\tan\frac{\tilde{z}_4\Theta}{2P}} \tag{13}$$

$$\rho_{cm} \approx \frac{r_m}{\tan\frac{\tilde{z}_5\Theta}{2P}} \tag{14}$$

$$\theta_{ecm} \approx \tilde{z}_1\frac{\Theta}{P} \tag{15}$$

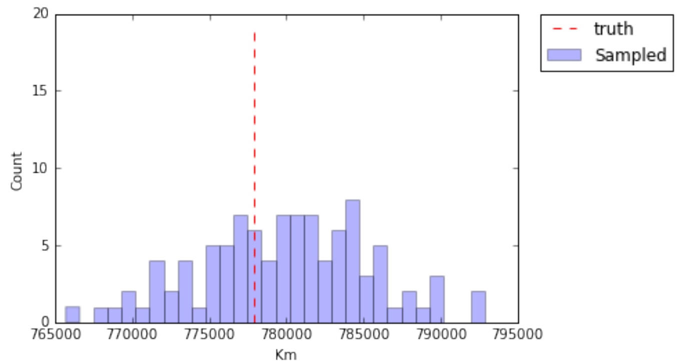

Figure 7. Probabilistic distribution for distance to Earth from batched measurements

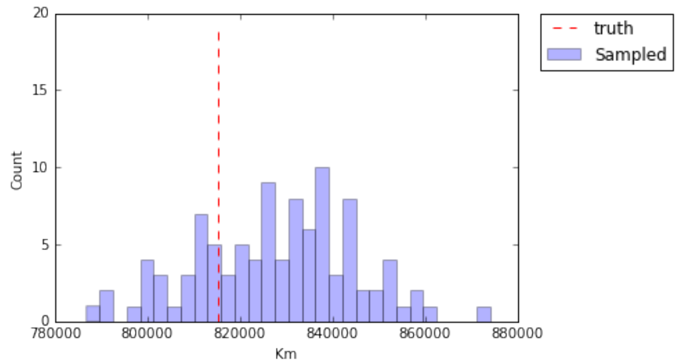

Figure 8. Probabilistic distribution for distance to Moon from batched measurements

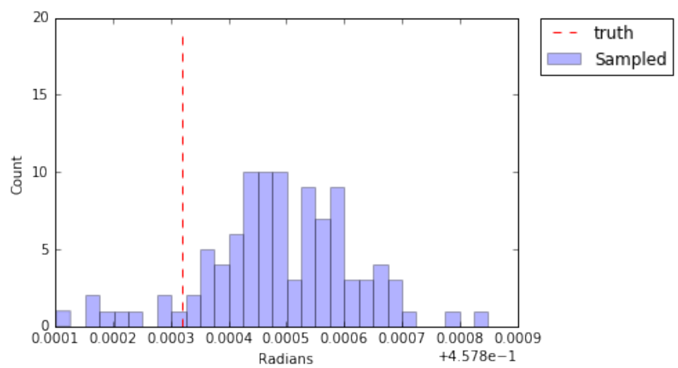

Figure 9. Probabilistic distribution for separating angle between Earth and Moon from batched measurements

Eqn (16) can be used to convert the distance and angular separation distributions into a distribution for separation distance between Earth and Moon, as shown in fig. 10. By comparing these approximated separation distances to the true separation distances that can be ascertained from the onboard ephemerides for the Earth and Moon, this distance measurement can be used to probabilitically isolate the spacecraft in time (fig. 11). These preliminary estimates need not and will not be particularly accurate. The goal is simply to reduce the searchspace to a discrete number of guesses. By subtracting the approximated separating distance from the true separation distances and finding all of the nearest approaches to zero, one arrives at a probabilistic distribution for time.

$$\rho_{em} \approx (\rho_{ce}^2 + \rho_{cm}^2 - 2\rho_{ce}\rho_{cm}\cos\theta_{ecm})^{\frac{1}{2}} \tag{16}$$

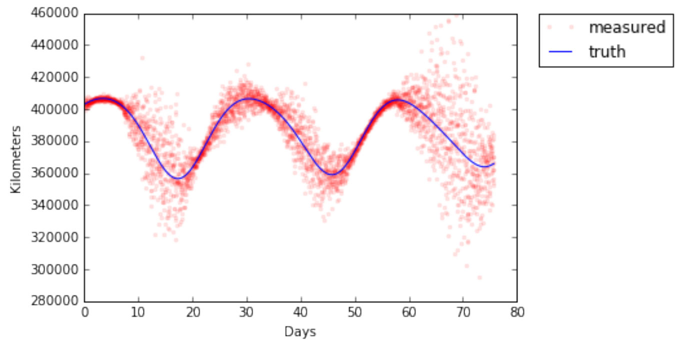

Figure 10. True and measured separation between Earth and Moon

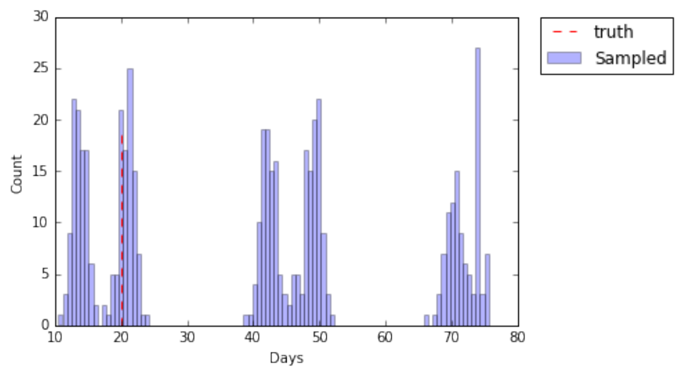

Figure 11. Probabilistic distribution for time from Earth-Moon separation, $t = 20$ days

The distributions for distance to Earth and Moon (figs. 7-8) and the distribution for separation distance between Earth and Moon (fig. 10) can also be used to isolate the spacecraft to a distribution of rings surrounding the line connecting the Earth and Moon. For each Earth-distance approximation, there is a sphere surrounding the Earth on which the spacecraft could reside. The same is true for the Moon distance approximations. The intersections of these spheres comprises a distribution of rings between the Earth and Moon that agree with the separation measurements. These rings are represented in terms of their x^e coordinate (the location of the center of the ring along the line from Earth to Moon) and their radius, r^e.

$$x^e = \frac{\rho_{em}^2 - \rho_{cm}^2 + \rho_{ce}^2}{2\rho_{em}} \tag{17}$$

$$r^e = \rho_{ce}^2 - (x^e)^2 \tag{18}$$

For each possible moment in time (given by fig. 11), the spacecraft may reside anywhere on the rings shown in figs. 12-13. From any of these locations in space and time, the expected measurements for Earth

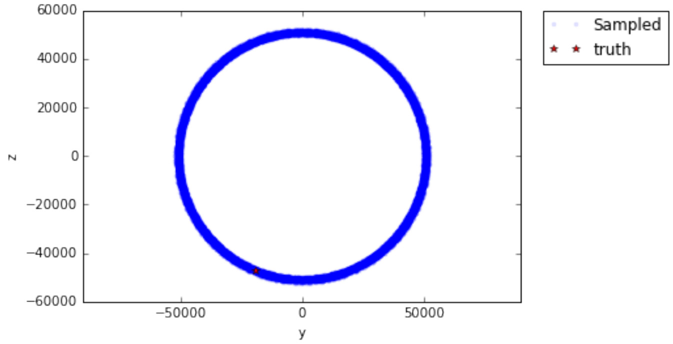

Figure 12. y^e, z^e **projection of distribution of rings of spacecraft positions**

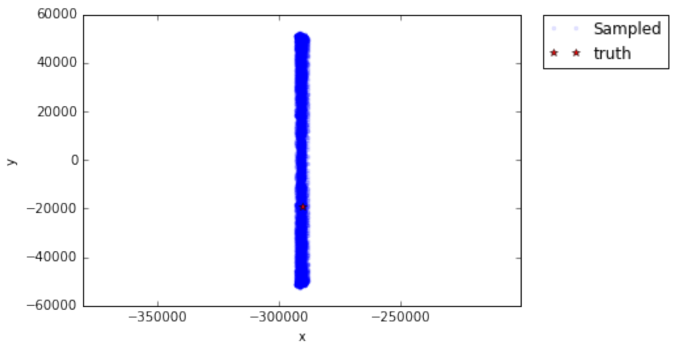

Figure 13. y^e, x^e **projection of distribution of rings of spacecraft positions**

width, Moon width, and Earth-Moon angle of separation will agree with those gathered. To narrow the searchspace down further, one can calculate the cost of each point in the ring distribution. Doing so includes information about the remaining two measurements: the Earth-Sun angle and the Moon-Sun angle. Fig. 14 shows the true position of the spacecraft in the ring and the least costly particle in the ring. The rest of the particles are plotted with an opacity in proportion to their cost. Consequently, there are two locations on the ring that agree with all measurements: one is above the plane formed by the Earth, Sun and Moon, and the other is symmetrically across that plane. This outcome is consistent with the results of Adams and Peck in [6]. For each possible moment in time, one can convert the least costly points in the ephemeral-frame ring into an ECI frame. Doing so yields the points in space and time that best agree with the gathered batch of measurements and reduces the searchspace to a series of clusters in space and time. For each moment in time, there is a pair of clusters (one cluster above the plane formed by the Earth, Sun, and Moon, and one symmetrically below that plane). If the mission lifetime were less than the orbital period of the moon, one would expect to find only two clusters. Since the mission under consideration in this analysis is long enough

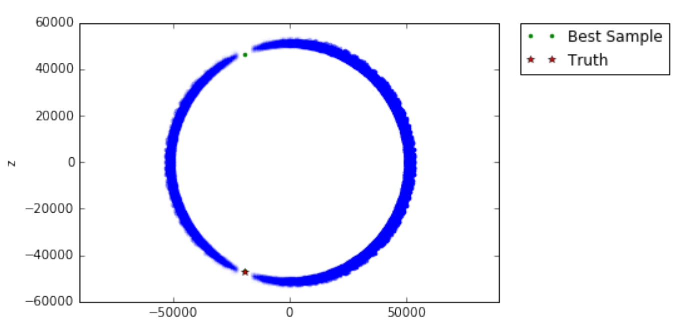

Figure 14. y^e, z^e **projection of distribution of rings of spacecraft positions**

to include multiple orbits of the moon around the Earth, one finds multiple pairs of clusters. The cluster that is nearest to a point on the planned spacecraft trajectory is used to instantiate a particle filter.

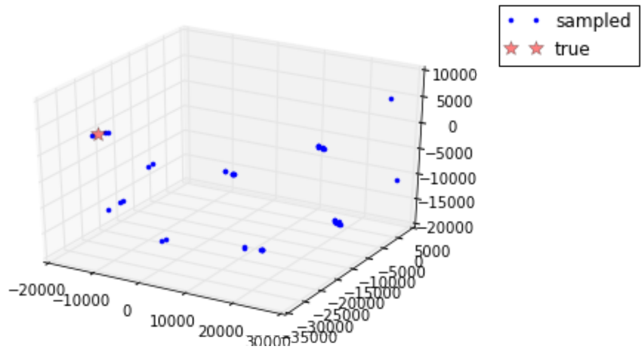

Figure 15. Reduced spacial searchspace, ECI frame

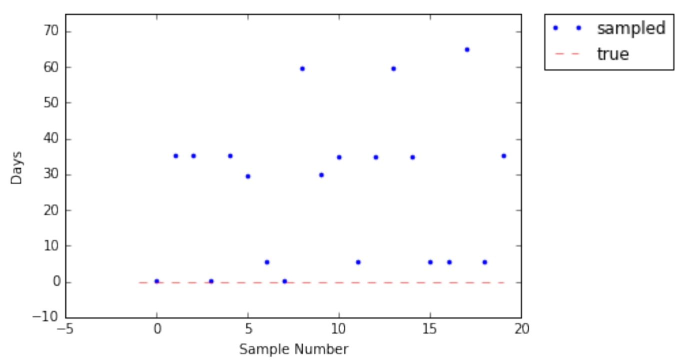

Figure 16. Reduced temporal searchspace

VI. Particle Filter

The seed from figs. 15-16 serves as the *a priori* $\hat{\mathbf{x}}(0)$ for the filter. From this seed, N_s particles are generated with Gaussian distributions in location, velocity, and time as shown in Eq (19). $N_s = 1000$ has been empirically determined to work well for this particular system. The initial covariance is set to a value large enough to ensure that some of the particles populate the correct region of the searchspace. A standard deviation of 8000 km for position, 5 km/sec for velocity, and 4 hours for time is used in this example. Initially, each particle is instantiated with equal weight, as shown in Eq (20). Each particle, which is characterized by a position, velocity, and time, is then propagated by numerically integrating its own dynamics model Eq (3-5), as shown in Eq (21). For this example, it is assumed that the camera system provides a new measurement every 1 minute.

$$\chi_i^0 = \mathcal{N}(\mathbf{x}_i(0), P(0)) \tag{19}$$

$$w_i^0 = \frac{1}{N_s} \tag{20}$$

$$\chi_i^1 = \mathbf{f}\left(\chi_i^0\right) \tag{21}$$

After the particles have been propagated to the next timestep, their weights are re-calculated. Because of the high gradients and size of the searchspace being traversed, a unique weighting method is required for the particle filter to converge. First, the measurement model combines the expected measurements associated with each propagated particle, and the innovation between each particle's expected measurement and the true measurement is calculated.

$$\nu_i^1 = \mathbf{z}^1 - \mathbf{h}(\chi_i^1) \tag{22}$$

If the innovations did not have the extremely wide range of values that are a feature of this system, one would calculate the weight of each particle by taking the exponential of the R-norm of the innovation. Instead, one can maintain better scaling on the weights by calculating the natural log of the exponential and adding the log of the previous weight.

$$log(w_i^1) = -\frac{1}{2}\left((\nu_i^1)^T R \nu_i^1\right) + log(w_i^0) \tag{23}$$

With this weighting convention, the greater the weight the better the particle is at anticipating the true measurement. It is possible that the weights calculated in Eq (23) will have a huge range of values. For computational safety, they can be rescaled by the maximum weight.

$$log(w_i^1) = \frac{log(w_i^1)}{max(log(w_i^1))} \tag{24}$$

Finally, one can find the minimum weight and rescale once more. The rescaled weights are given by the exponential of the difference between each weight and the minimum weight.

$$w_i^1 = e^{min(log(w_i^1)) - log(w_i^1)} \tag{25}$$

The result is that better particles have greater weight, and worse particles have lesser weight. The updated state and covariance estimates are given by the weighted average of the propagated particles. The effective number of particles can be calculated using Eq (28).

$$\hat{\mathbf{x}}(1) = \sum_{k=0}^{N_s} w_i^1 \chi_i^1 \tag{26}$$

$$P(1) = \sum_{k=0}^{N_s} w_i^1 \left(\chi_i^1 - \hat{\mathbf{x}}(1)\right)\left(\chi_i^1 - \hat{\mathbf{x}}(1)\right)^T \tag{27}$$

$$N_{eff} = \frac{1}{\sum_{k=0}^{N_s} (w_i^1)^2} \tag{28}$$

If the effective number of particles is greater than the resampling threshold, N_t, then the particles retain their weights and are propagated again to repeat the above cycle for the next timestep. In this analysis, $N_t = 200$. If not, then the particles are resampled and their weights are reset according to Eq (20). The nature of this problem calls for a somewhat unique method for resampling. In a conventional problem, one uses roulette selection to probabilistically resample particles, resulting in multiple copies of high-weight particles and fewer (or zero) copies of low-weight particles. The repeated high-weight particles are then spread out via process noise and dithering by sampling from an Epanechnikov kernel function. For this particular problem, that method of resampling does not work reliably. Because the measurements depend only on position and time (and not on velocity), information must accumulate for a number of timesteps in order to learn anything about the spacecraft's velocity. By instead resampling such that the spacecraft's position is driven almost entirely by the velocity, one can more quickly converge on the correct answer.

In the event that the number of effective particles below the threshold, the particles are replaced with a new set. The position and time states for each of these new particles are given by the current position and time estimates. The velocity for each particle is sampled from a multivariate Gaussian distribution with a mean of the latest velocity estimate and a covariance of the sum of the error covariance estimate and the process noise covariance. In order to maintain diversity, the process noise covariance for the velocity states is kept relatively large (2 km/sec). This resampling procedure is summarized in Eq (29-30). After resampling, the particles are again propagated according to Eq (21), a new measurement is gathered, and the process is repeated.

$$\chi_i^1 = \begin{bmatrix} \hat{x}(1) & \hat{y}(1) & \hat{z}(1) & \mathcal{N}\left(\begin{bmatrix}\hat{\dot{x}}(1)\\ \hat{\dot{y}}(1)\\ \hat{\dot{z}}(1)\end{bmatrix}, P(1)+Q\right) & \hat{t}(1) & \hat{t_0}(1)\end{bmatrix}^T \tag{29}$$

$$w_i^1 = \frac{1}{N_s} \tag{30}$$

VII. Results

For the case shown in figs. 15-16, the cluster found to be nearest to the true trajectory (2-norm of error vector in time and space) is the cluster nearest the red star of fig. 15, as expected. A point in this cluster is used to seed a particle filter as described in Section VI. The filter converges to within tens of kilometers of the true spacecraft position, tenths of kilometers per second of true spacecraft velocity, and tens of minutes of the true time in approximately 500 seconds, as shown in figs. 17-20. In fig. 17, more recent estimates have greater opacity than older estimates.

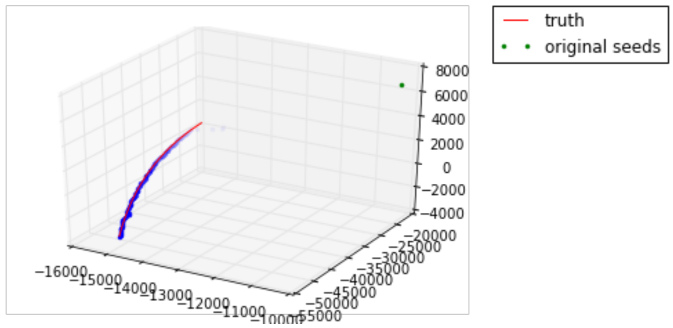

Figure 17. True and estimated spacecraft trajectory

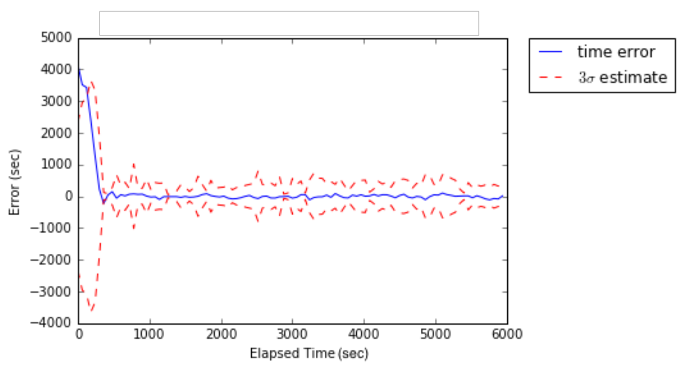

Figure 18. Error in estimated time

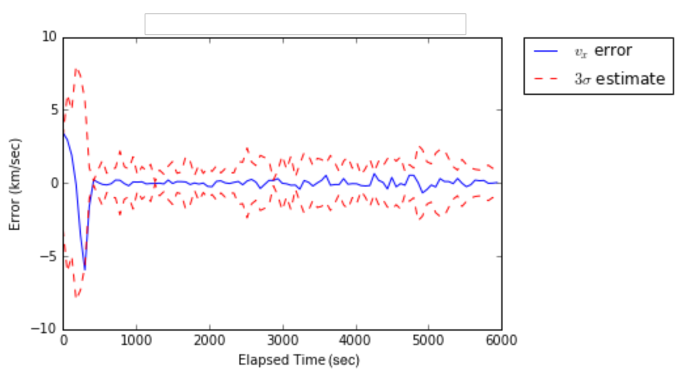

Figure 19. Error in estimated z-velocity

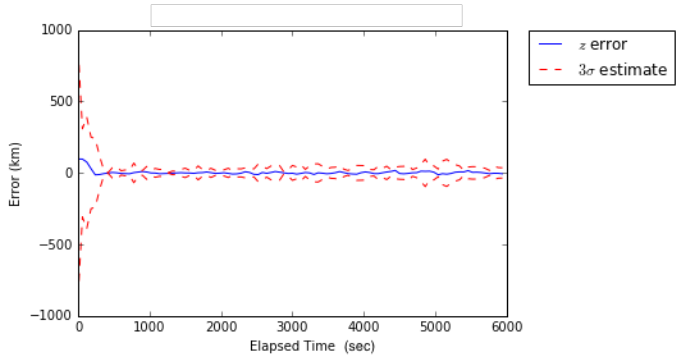

Figure 20. Error in estimated z-position

VIII. Conclusion and Future Work

This analysis shows that a spacecraft in cislunar space equipped with a simple vision system, a relative clock, ephemeris tables for the Earth, Sun, and Moon and a basic knowledge of planned mission can use optical measurements to recover its trajectory and time to within tens of kilometers and tens of minutes. The spacecraft uses batched measurements to reduce the searchspace to a number of discrete points in space and time, and then uses the point nearest to its own nominal trajectory to instantiate a particle filter.

In the absence of any knowledge of a planned trajectory, the spacecraft has no means of preferring one of the seeds shown in figs. 15-16 over any of the others. As discussed in Section V, a mission lifetime shorter than the orbital period of the moon would result in only two clusters and two possible trajectories. Each of these trajectories would converge to the same time. On timescales less than the orbital period of the Moon, one can solve the lost-in-time problem without strictly solving the lost-in-space problem.

The mission under consideration in this analysis includes multiple orbits of the Moon, resulting in multiple pairs of trajectories, as shown in fig. 21. Anothert case of interest is one in which the spacecraft has no knowledge whatsoever of its own planned mission, which may include many orbits of the Moon around the Earth. In this case, the spacecraft needs to select a single trajectory based on its properties (conservation of specific angular momentum or specific orbital energy, for example, in the two-body case). Future work will involve developing a procedure for selecting the true trajectory among all possible trajectories shown in fig. 21.

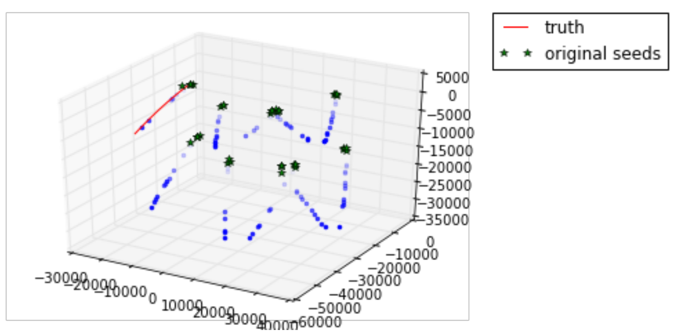

Figure 21. All trajectories from all seeds

Acknowledgments

The authors thank Professor Mark Psiaki for his input with regard to the particle filter associated with this research.

References

[1]Bhaskaran, Shyam, et al. "Orbit determination performance evaluation of the deep space 1 autonomous navigation system." AIAA/AAS Space Flight Mechanics Meeting, Monterey. 1998.

[2]Glenn E. Lightsey and John A. Christian. "Onboard Image-Processing Algorithm for a Spacecraft Optical Navigation Sensor System", Journal of Spacecraft and Rockets, Vol. 49, No. 2 (2012), pp. 337-352. http://dx.doi.org/10.2514/1.A32065

[3]John A. Christian. "Autonomous Navigation System Performance in the Earth-Moon System", AIAA SPACE 2013 Conference and Exposition, SPACE Conferences and Exposition, http://dx.doi.org/10.2514/6.2013-5496

[4]Manchester, Zachary, Mason Peck, and Andrew Filo. "Kicksat: A crowd-funded mission to demonstrate the worlds smallest spacecraft." (2013).

[5]Small Spacecraft Technology State of the Art, NASA/TP 2014 216648/rev1, Ames Research Center, Moffett Field, CA.

[6]Van H. Adams and Mason A. Peck. "Interplanetary Optical Navigation", AIAA Guidance, Navigation, and Control Conference, AIAA SciTech, http://dx.doi.org/10.2514/6.2016-2093